Pergamon

Int. J. Heat Mass Transfer. Vol. 40, No. 11, pp. 2607–2620, 1997

Printed in Great Britain
0017–9310/97 $17.00+0.00

PII: S0017-9310(96)00282-7

Role of gas-phase reaction and gas–solid thermal nonequilibrium in reverse combustion

M. FATEHI and M. KAVIANY†

Department of Mechanical Engineering and Applied Mechanics, The University of Michigan, Ann Arbor, MI 48109-2125, U.S.A.

(*Received* 1 *July* 1996 *and in final form* 5 *August* 1996)

Abstract—The process of adiabatic reverse combustion when air is supplied through a packed bed of wood particles is analyzed in the oxygen-limited regime when both the gas-phase homogeneous reaction and the gas–solid surface reaction are significant. This is an extension of an earlier study where the gas–solid surface reaction was assumed dominant and the local thermal equilibrium was assumed between the gas and solid phases (i.e. the single-medium model). Here allowance is made for the local thermal and chemical nonequilibria between the phases (i.e. the two-medium model) and the model is used to describe the propagation of the reaction front through the fuel bed. The role of the air pore velocity and the homogeneous reaction rate in the front speed, the adiabatic final temperature, the degree of solid consumption and the unburnt volatiles concentration in the post gas-phase oxidation region, are examined parametrically. The volumetric solid-phase pyrolysis is considered to be the mechanism producing the volatile fuel. First-order Arrhenius kinetics are used in the single-step reaction models. It is found that the gas-phase reaction becomes dominant over the heterogeneous reaction at high air pore velocities, thus reducing the degree of solid consumption. These predictions are in agreement with the earlier experimental results and the predicted results of the single-medium treatment.

1. INTRODUCTION

Propagation of the burning front in combustible porous solids can be self-sustained when a sufficient portion of the heat of combustion is transported to the nonreacted fuel primarily for preheating. In reverse combustion of porous materials, gaseous oxidant flows opposite to the direction of the combustion wave with the gas- and solid-phase temperature rising in the preheat region ahead of the burning front. For low oxidant flow rates, only the solid-phase reaction occurs (smoldering). At higher flow rates, resulting in an increase in the temperature of the gas and solid, transition to flaming takes place. There are numerous industrial applications that qualitatively resemble reverse combustion. Amongst the most relevant are the *in situ* coal gasification, underground oil recovery, fixed-bed catalytic reactors, high-temperature materials synthesis, incineration of solid waste, biomass combustion and fire spread. Some of these processes involve combustion in porous media in the absence of flaming. Others such as incineration and fire spread involve chemical reactions both in the gas and solid phases. In one of the models of *in situ* coal combustion, the gas-phase oxidation of vaporized fuel is the primary exothermic reaction.

Numerous studies on the pyrolysis and combustion of materials that can sustain smoldering have been reported. Palmer [1] provides an earlier review on the smoldering. The transition to flaming through the forced flow of oxygen is studied experimentally by Ohlemiller [2, 3] and Rogers and Ohlemiller [4]. Moussa *et al.* [5] experimentally and theoretically examine the mechanism of smoldering in cellulosic materials. Dosanjh *et al.* [6] and Schult *et al.* [7] present analytical models for reverse smolder using the method of large activation energy asymptotics. Related work is performed by Robinovich and Gurevich [8] in the context of high temperature materials synthesis. Britten and Krantz [9, 10] apply the linear stability theory to the reverse smolder by considering both heterogeneous and gas-phase oxidations. Fatehi and Kaviany [11] investigate reverse combustion in a packed bed of wood particles assuming heterogeneous reactions as the dominant reaction mechanism and also perform experiments. Lozinski and Buckmaster [12] recently study the quenching of reverse smolder as a consequence of endothermic post-oxidative pyrolysis.

Most of the theoretical studies consider systems which are far from stoichiometry (i.e. oxidant limited) such that the solid fuel concentration has negligible impact on the reaction rate. These studies are conducted solely for the smoldering combustion at low oxidant flow rates. Even at high oxidant flow rate processes (which are fuel limited), the gas-phase oxidation is usually neglected. For some substances that can sustain smoldering (e.g. wood, cellulosic materials and polymeric foams), a fuel-limited regime (without

† Author to whom correspondence should be addressed.

NOMENCLATURE

A	pre-exponential factor [s^{-1}]
A_{sg}	solid–gas surface area [m^{-1}]
c_p	specific heat capacity [J kg K^{-1}]
d_p	diameter [m]
D	molecular mass diffusivity [m^2 s^{-1}]
$D^d_{m_{xx}}$	axial mass dispersion coefficient [m^2 s^{-1}]
D^d_{xx}	axial thermal dispersion coefficient [m^2 s^{-1}]
ΔE_a	activation energy for reaction [J $mole^{-1}$]
F	radiation exchange factor
g	gravitational constant [m s^{-2}]
h_{sq}	interstitial heat transfer coefficient [W m^{-2} K^{-1}]
Δi	heat of combustion [J kg^{-1}]
k	thermal conductivity [W m K^{-1}]
n_r	number of components
$\dot{n}_d$	diffusion-controlled reaction rate [kg m^{-3} s^{-1}]
$\dot{n}_{\Delta E}$	kinetically-controlled reaction rate [kg m^{-3} s^{-1}]
$\dot{n}$	reaction rate [kg m^{-3} s^{-1}]
$\langle Nu_d \rangle_{sg}$	Nusselt number
Pe	Peclet number
Pr	Prandtl number
Re	Reynolds number
R_g	gas constant [J mol K^{-1}]
Sc	Schmidt number
$\langle Sh_d \rangle_{sg}$	Sherwood number
t	time [s]
T	temperature [K]
u	velocity [m s^{-1}]
V	representative elementary volume [m^3]
x	spatial coordinate [m]
x_l	moving spatial coordinate [m].

Greek symbols

α	thermal diffusivity [m^2 s^{-1}]
β	volatile depletion coefficient
ε	porosity
ε_r	surface emissivity
η	conversion factor
δ_F	combustion-front thickness [m]
ρ	density [kg m^{-3}]
σ	Stefan–Boltzmann constant [W m^{-2} K^{-4}]
v	kinematic viscosity [m^2 s^{-1}] or stoichiometric coefficient.

Superscripts

d	dispersion
g	gas
s	solid.

Subscripts

a	ash
c	char
cd,p	products in condensed phase
D	Darcean
e	effective
f	final
F	front
g	gas
gs	gas–solid interface
gp	gaseous products
hom	homogeneous
i	species
m	maximum
n	nonreacted
o	oxygen
p	pyrolysis
pyr	pyrolytic reaction
r	reacted, or radiation
s	solid
st	stoichiometric
t	heat
v	volatile
x	x-coordinate.

transition to flaming) does not occur unless homogeneous reactions are suppressed with the use of fire retardants.

The main objective of the present analysis is to study the effect of a significant gas-phase oxidation at high temperatures (i.e. flaming) on the reverse combustion in porous media. The propagation speed, the maximum attainable local temperature (which can be larger than the adiabatic temperature) and the degree of solid consumption, are of primary interest. It is generally believed that exothermicity of gas-phase oxidation at low temperatures does not generate the heat required for sustained smoldering. Surface char oxidation and/or oxidative solid degradation are often attributed to the primary mechanism, of the front propagation. From chemical considerations, the solid surface suppresses the chain reactions of the free radicals due to the third body recombination of the radicals. In a packed bed, the gas-phase reactions can be inhibited because of a large specific area of the solid.

The full chemistry for the reactions in noninert porous media is generally not known for most materials. In this respect, some simplifications in modeling the chemistry of combustion must be made. A three-step reaction mechanism for gas/solid reactions is proposed by Ohlemiller [13] as: (i) endothermic pyrolysis; (ii) exothermic thermal degra-

dation; and (iii) exothermic char oxidation. The second reaction stage (exothermic solid decomposition) is used by several investigators to model the reverse smolder in cellulosic and polymeric substances. Kashiwagi and Nambu [14] provide the kinetic rates for the pyrolysis, oxidative thermal degradation and char oxidation of cellulosic materials. Shafizadeh [15] presents two alternative pathways for the decomposition of wood to: (i) volatiles; and (ii) char and gaseous products. The kinetic constants for each pathway are also reported by Shafizadeh. A simplified reaction scheme for the gas/solid surface reactions used by Dosanjh *et al.* [6] and Schult *et al.* [7] assumes a one-step reaction model in the form

$$1\ \text{g(unburnt solid)} + \nu_0 O_2 \rightarrow \nu_{cd,p}(\text{condensed-phase products}) + \nu_{gp}(\text{gaseous products}). \quad (1)$$

The above reaction mechanism is used in the present analysis with the consideration that the ash content of the products is negligible (i.e. $\nu_{cd,p} = 0$). For wood, the ash content is normally less than 1%. Since here the focus is on the role of homogeneous reactions on the reverse combustion, the volumetric pyrolysis is considered to be endothermic. For the high temperatures encountered during the reverse combustion in the presence of flaming, the oxygen penetration through the particle for the oxidative pyrolysis is considered to be insignificant. In fact, oxygen concentration is limited to the external surface of the particle, where it is consumed based on the heterogeneous reaction rate.

Wood pyrolysis results in the formation of volatiles of varying compounds. Gaseous formaldehyde appears to be an appropriate choice in representing an average pyrolysis product based on the mole and energy balances (Kosdon *et al.* [16]). The atomic ratios in the formaldehyde and dehydrocellulose are the same, and the heat of reaction of the formaldehyde is nearly equal to that on an equimolar mixture of CO and H_2. The gas-phase reaction is therefore modeled as

$$CH_2 = O + O_2 \rightarrow H_2O + CO_2. \quad (2)$$

Although the gas-phase reactions may play a secondary role in the smoldering combustion for low air flow rates, the transition to intense flaming (which occurs at high flow rates) indicates the necessity to include the homogeneous reactions in the models. Acknowledging the complexity of the detailed chemistry and kinetics present in these reactions, here an attempt is made to predict the global features of the reverse combustion (albeit with simplified kinetic models), by considering the interplay between the chemical and thermophysical processes controlling the sustained propagation.

2. ANALYSIS

Figure 1 illustrates the coexisting gas and solid-phase reactions in a combusting porous medium. The porous medium consists of a packed bed of randomly arranged spherical wood particles. The upward flow of the air ($\langle\rho_0\rangle_n^g/\langle\rho\rangle_n^g = 0.23$) against the gravitational field is in the opposite direction to that of the combustion wave propagating downward through the porous medium. The thermobuoyant flow in such a configuration is assumed negligible compared to the forced air flow rates required for the self-sustained propagation.

The reaction front is assumed to be planar and propagate at a constant speed. This speed is determined by the balance between the rate of heat generation (due to exothermic reactions in the solid and gas) and the upstream transport of this heat to the nonreacted solid fuel and the incoming gas. The solid can undergo pyrolysis generating the volatile fuel to react with the oxygen available in the gas phase. Heterogeneous reactions can take place concurrently with the gas-phase reactions. The extent of the surface reactions depend on the rate of the oxygen diffusion to the surface of the char produced subsequent to the pyrolysis of wood. A schematic of the process is presented in Fig. 2 to identify different reaction regions, the reaction front structure and pore-level considerations given to the present analysis, As shown in Fig. 2, the distinct regions exist: heating and drying of the wood particles; pyrolysis; char oxidation; and gas-phase reaction region (flaming). For a given fuel bed porosity and particle size, the intensity, relative position and width of the reaction regions are not known *a priori* and can vary greatly depending on the flow rate of the incoming gas, the initial concentration of the oxygen on the flow and the chemical kinetics and thermal effects.

The two-medium treatment uses the local volume-averaged model allowing for the thermal and chemical nonequilibria between the solid and the gas phase. In this study, the temperature and the species gradients in the condense phase are assumed to be negligible. The solid phase is treated as a continuum on the scale of the combustion wave and the particle-scale gradients are excluded. For large size particles and fast moving reaction fronts (short residence time compared to the particle heating time), the temperature nonuniformity in the particle becomes important. This is especially true when the heat transfer across the thermal boundary layer in the gas phase is much larger than the heat transport by conduction in the solid phase (i.e. large Biot number). In this study the following additional assumptions are made: (i) the volumetric effective conductivities of the solid medium $[(1-\varepsilon)\langle k\rangle^s]$, and that for the has medium $(\varepsilon\langle k\rangle^g)$, are constant; (ii) the specific heat capacities for the gas and solid phases are independent of the temperature variations; (iii) the effective mass diffusivity of the various species in the gas phase is the same for all

species; (iv) $\langle\rho\rangle^g\langle D\rangle^g$ remains constant; (v) the process is adiabatic; (vi) the fuel bed is long enough such that the end effects are negligible; (vii) the temperature and species gradients far upstream and downstream of the reaction front are zero; and (viii) moisture content of the solid is negligible. Moreover, the effect of the particle shrinkage on the reverse combustion is not included in the present formulations.

2.1. *Governing equations*

The energy equations for the gas and solid phases are (Kaviany [17])

$$\frac{\partial}{\partial t}[\varepsilon\langle\rho c_p\rangle^g\langle T\rangle^g]+\frac{\partial}{\partial x}[\varepsilon\langle\rho c_p\rangle^g\langle u\rangle^g\langle T\rangle^g]$$
$$=\frac{\partial}{\partial x}\left\{\varepsilon[\langle k\rangle^g+\langle\rho c_p\rangle^g D^d_{xx}]\frac{\partial\langle T\rangle^g}{\partial x}\right\}$$
$$+\frac{\langle Nu_d\rangle A_{sg}\langle k\rangle^g}{d_p}\frac{A_{sg}}{V}(\langle T\rangle^s-\langle T\rangle^g)$$
$$+\Delta i_{v,g}\langle\dot n_{v,g}\rangle\frac{\partial}{\partial t}[(1-\varepsilon)\langle\rho c_p\rangle^s\langle T\rangle^s]$$
$$=\frac{\partial}{\partial x}\left\{[(1-\varepsilon)\langle k\rangle^s+\langle k_r\rangle^s]\frac{\partial\langle T\rangle^s}{\partial x}\right\} \quad (3)$$

$$-\frac{\langle Nu_d\rangle A_{sg}\langle k\rangle^g}{d_p}\frac{A_{sg}}{V}(\langle T\rangle^s-\langle T\rangle^g)$$
$$+\Delta i_{v,s}\langle\dot n_{v,s}\rangle+\Delta i_{c,s}\langle\dot n_{c,s}\rangle. \quad (4)$$

The symbols $\langle\,\rangle^g$ and $\langle\,\rangle^s$ represent local, phase volume-averaged quantities over the gas V_g and solid V_s volumes in the representative elementary volume, respectively. The volumetric reaction rate for the volatiles in the bulk gas phase $\langle\dot n_{v,g}\rangle$, is local volume averaged over the representative elementary volume (i.e. $V=V_g+V_s$). The volumetric rate of the solid pyrolysis $\langle\dot n_{v,s}\rangle$ and the char oxidation $\langle\dot n_{c,s}\rangle$, in the bulk solid-phase, are also local volume averaged over the representative elementary volume.

The conservation of species in the gas phase is given by

$$\frac{\partial}{\partial t}(\varepsilon\langle\rho_i\rangle^g)+\frac{\partial}{\partial x}(\varepsilon\langle u\rangle^g\langle\rho_i\rangle^g$$
$$=\frac{\partial}{\partial x}\left[\varepsilon(\langle D\rangle^g+D^d_{m_{xx}})\langle\rho\rangle^g\frac{\partial\langle\rho_i\rangle^g/\langle\rho\rangle^g}{\partial x}\right]$$
$$+\langle\dot n_{i,g}\rangle+\langle\dot n_{i,gs}\rangle, \quad (5)$$

where i denotes oxygen o, volatile fuel v, or gaseous products gp. The consumption species i as a result of homogeneous reactions and the production of species i (which is allowed only for the volatile fuel component v) as a result of the pyrolysis in the solid-phase, are represented by the overall reaction rate in the gas-phase $\langle\dot n_{i,g}\rangle$. The production or consumption of species i due to heterogeneous reactions are represented by $\langle\dot n_{i,gs}\rangle$.

The conservation of mass in the bulk gas phase is written as

$$\frac{\partial}{\partial t}(\varepsilon\langle\rho\rangle^g)+\frac{\partial}{\partial x}(\varepsilon\langle\rho\rangle^g\langle u\rangle^g)=\sum_{i=1}^{n_{rg}}\langle\dot n_{i,g}\rangle+\sum_{i=1}^{n_{rg}}\langle\dot n_{i,gs}\rangle. \quad (6)$$

The conservation equation for the bulk solid phase is given by

$$\frac{\partial}{\partial t}[(1-\varepsilon)\langle\rho\rangle^s]=\sum_{i=1}^{n_{rs}}\langle\dot n_{i,s}\rangle, \quad (7)$$

where n_{rg} and n_{rs} are the number of components in the gas and solid phases.

For the position of the char reaction front given by $x_f=x(t)$, a coordinate system fixed to this front is given by $x_1=x_f-x(t)$. The solid and the gas enter the reaction zone at a speed of $u_F=-\mathrm{d}x/\mathrm{d}t$ and $\langle u\rangle^g+u_F$, respectively. The governing equations for conservation of energy and species [equations (3)–(7)] are then transformed and written with respect to the new coordinate system x_1 fixed at the reaction front. The gas-phase energy equation is

$$\frac{\mathrm{d}}{\mathrm{d}x_1}[\varepsilon\langle\rho c_p\rangle^g(\langle u\rangle^g+u_F)\langle T\rangle^g]$$
$$=\frac{\mathrm{d}}{\mathrm{d}x_1}\left\{\varepsilon[\langle k\rangle^g+\langle\rho c_p\rangle^g D^d_{xx}]\frac{\mathrm{d}\langle T\rangle^g}{\mathrm{d}x_1}\right\}$$
$$+\frac{\langle Nu_d\rangle A_{sg}\langle k\rangle^g}{d_p}\frac{A_{sg}}{V}(\langle T\rangle^s-\langle T\rangle^g)+\Delta i_{v,g}\langle\dot n_{v,g}\rangle. \quad (8)$$

The solid-phase energy equation is

$$\frac{\mathrm{d}}{\mathrm{d}x_1}[(1-\varepsilon)\langle\rho c_p\rangle^s u_F\langle T\rangle^s]$$
$$=\frac{\mathrm{d}}{\mathrm{d}x_1}\left\{[(1-\varepsilon)\langle k\rangle^s+\langle k_r\rangle^s]\frac{\mathrm{d}\langle T\rangle^s}{\mathrm{d}x_1}\right\}$$
$$-\frac{\langle Nu_d\rangle A_{sg}\langle k\rangle^g}{d_p}\frac{A_{sg}}{V}(\langle T\rangle^s-\langle T\rangle^g)$$
$$+\Delta i_{v,s}\langle\dot n_{v,s}\rangle+\Delta i_{c,s}\langle\dot n_{c,s}\rangle. \quad (9)$$

The conservation of gaseous species is

$$\frac{\mathrm{d}}{\mathrm{d}x_1}[\varepsilon(\langle u\rangle^g+u_F)\langle\rho_i\rangle^g$$
$$=\frac{\mathrm{d}}{\mathrm{d}x_1}\left[\varepsilon(\langle D\rangle^g+D^d_{m_{xx}})\langle\rho\rangle^g\frac{d\langle\rho_i\rangle^g/\langle\rho\rangle^g}{\mathrm{d}x_1}\right]$$
$$+\langle\dot n_{i,g}\rangle+\langle\dot n_{i,gs}\rangle. \quad (10)$$

The conservation of mass in the bulk phase is

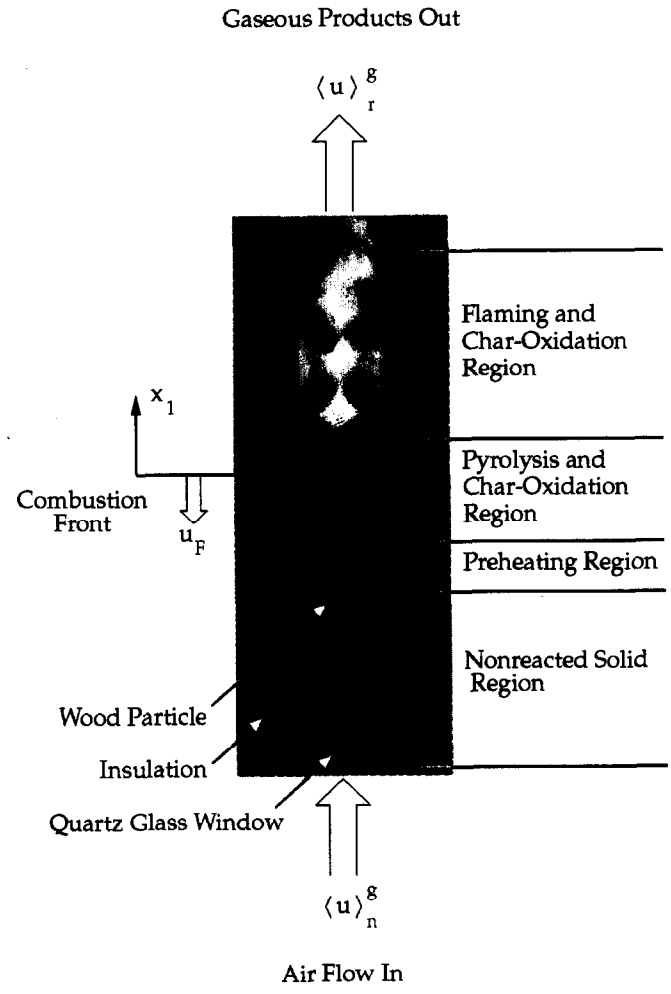

Fig. 1. Photograph of the propagation of the burning front in a packed bed of wood particles showing solid surface and gas-phase reactions. The different regions are defined.

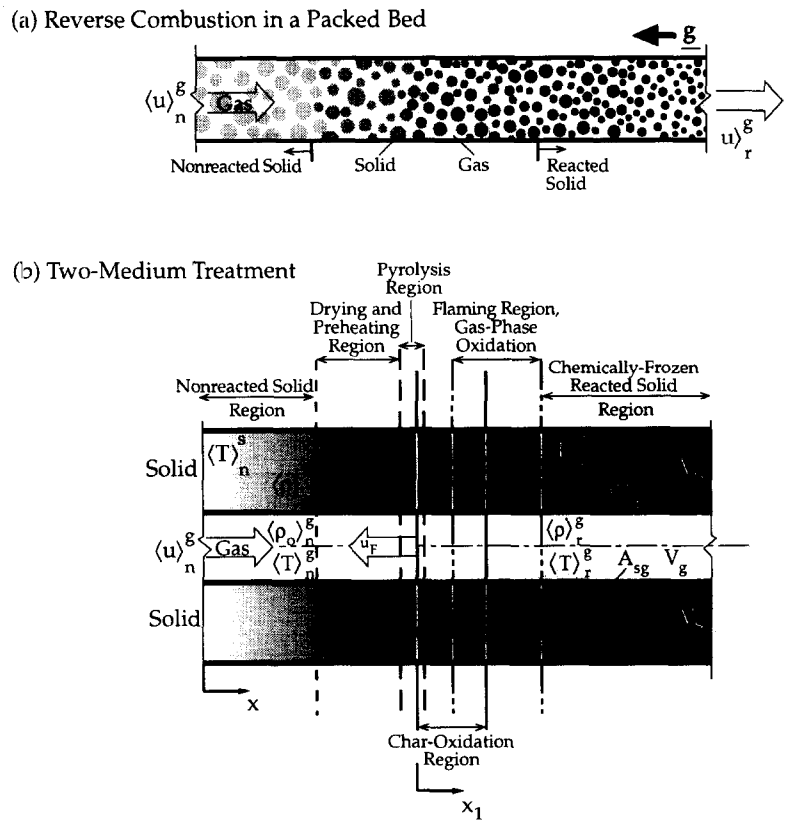

Fig. 2. Schematic of reverse combustion and reaction front structure: (a) direction of air flow and gravity vector; (b) two-medium model for solid and gas phases; (c) local volume-averaged structure of reaction front; and (d) a pore-level rendering of the structure.

$$\frac{\mathrm{d}}{\mathrm{d}x_1}[\varepsilon\langle\rho\rangle^{\mathrm{g}}(\langle u\rangle^{\mathrm{g}}+u_{\mathrm{F}})] = \sum_{i=1}^{n_{\mathrm{rg}}}\langle\dot{n}_{i,\mathrm{g}}\rangle. \quad (11)$$

The conservation of species in the solid phase $[\langle\rho\rangle^{\mathrm{s}} = \langle\rho_{\mathrm{v}}\rangle^{\mathrm{s}}+\langle\rho_{\mathrm{c}}\rangle^{\mathrm{s}}]$ is

$$\frac{\mathrm{d}}{\mathrm{d}x_1}[(1-\varepsilon)\langle\rho_i\rangle^{\mathrm{s}}u_{\mathrm{F}}] = \langle\dot{n}_{i,\mathrm{s}}\rangle, \quad (12)$$

where i denotes the volatile v or the char c in the solid phase.

Defining the degree of the solid consumption to pyrolysis and char oxidation as $\eta = 1-\langle\rho\rangle^{\mathrm{s}}/\langle\rho\rangle^{\mathrm{s}}_{\mathrm{n}}$, where $\langle\rho\rangle^{\mathrm{s}}_{\mathrm{n}}$ is the density of the nonreacted solid fuel, the conservation of mass in the bulk solid phase is written as

$$\frac{\mathrm{d}}{\mathrm{d}x_1}[(1-\varepsilon)\langle\rho\rangle^{\mathrm{s}}_{\mathrm{n}}(1-\eta)u_{\mathrm{F}}] = \sum_{i=1}^{n_{\mathrm{rs}}}\langle\dot{n}_{i,\mathrm{s}}\rangle. \quad (13)$$

For the momentum equation, it is assumed that the pressure drop across the burning front is negligible (i.e. high permeability) and then only the gas-phase continuity equation is considered.

2.2. *Reaction kinetics models*†

A simple reaction kinetics model is used for the volumetric solid phase pyrolysis†

$$\langle\dot{n}_{\mathrm{v,s}}\rangle = -A_{\mathrm{p}}\langle\rho_{\mathrm{v,s}}\rangle_{\mathrm{n}}(1-\beta)^{n}\exp\left(-\frac{\Delta E_{\mathrm{a,p}}}{R_{\mathrm{g}}\langle T\rangle^{\mathrm{s}}}\right), \quad (14)$$

where $\beta = 1-\langle\rho_{\mathrm{v}}\rangle^{\mathrm{s}}/\langle\rho_{\mathrm{v}}\rangle^{\mathrm{s}}_{\mathrm{n}}$ and $\langle\rho_{\mathrm{v}}\rangle^{\mathrm{s}}_{\mathrm{n}}$ is the volatile content of the solid fuel in the nonreacted region. The reaction rate for the pyrolysis is modeled in such a way that pyrolysis terminates upon a complete depletion of the volatiles from the solid phase (i.e. $\langle\rho_{\mathrm{v}}\rangle^{\mathrm{s}} \to 0$ when $\beta \to 1$).

The surface (i.e. heterogeneous) reaction (as a result of the oxygen attack on the solid surface) is modeled in the form of Arrhenius reaction as

$$\langle\dot{n}_{\mathrm{c,s}}\rangle_{\Delta E} = A_{\mathrm{c}}\langle\rho_{\mathrm{o,gs}}\rangle\langle\rho_{\mathrm{c,s}}\rangle\exp\left(-\frac{\Delta E_{\mathrm{a,c}}}{R_{\mathrm{g}}\langle T\rangle^{\mathrm{s}}}\right). \quad (15)$$

At low temperatures, the heterogeneous reactions are kinetically controlled and because of the higher rate of the oxygen diffusion to the surfacer of the particle, the difference between the concentration of the oxygen at the gas/solid interface and the bulk gas phase is small (i.e. $\langle\rho_{\mathrm{o,gs}}\rangle \simeq \langle\rho_{\mathrm{o,g}}\rangle$). At high temperatures, the reaction rate is expected to be so fast that the rate-controlling path for the solid/oxygen reaction is the diffusion rate of the oxygen from the bulk gas to the surface of the solid particle. Due to the high temperatures at the surface and the fast kinetics, oxygen will be immediately consumed at the surface of the particle such that $\langle\rho_{\mathrm{o,gs}}\rangle = 0$. For the mass-diffusion controlled reactions, the heterogeneous reaction rate can be written as

$$\langle\dot{n}_{\mathrm{c,s}}\rangle = -\frac{\langle Sh_{\mathrm{d}}\rangle A_{\mathrm{gs}}\langle D_{\mathrm{m}}\rangle^{\mathrm{g}}}{\varepsilon d_{\mathrm{p}}}\frac{A_{\mathrm{gs}}}{V}(\langle\rho_{\mathrm{o,g}}\rangle-\langle\rho_{\mathrm{o,gs}}\rangle), \quad (16)$$

where $\langle\rho_{\mathrm{o}}\rangle^{\mathrm{g}} \gg \langle\rho_{\mathrm{o}}\rangle^{\mathrm{gs}}$ for fast kinetics. Mass diffusion to the particle surface is modeled using the solid–gas mass transfer coefficient $\langle Sh_{\mathrm{d}}\rangle A_{\mathrm{gs}}$. The overall, local volume-averaged heterogeneous reaction rate can therefore be modified as

$$\langle\dot{n}_{\mathrm{c,s}}\rangle = \frac{1}{\dfrac{1}{\langle\dot{n}_{\mathrm{c,s}}\rangle_{D}}+\dfrac{1}{\langle\dot{n}_{\mathrm{c,s}}\rangle_{\Delta E}}}. \quad (17)$$

The above equation represents two distinct reaction regimes at the high and low temperatures, namely,

$$\langle\dot{n}_{\mathrm{c,s}}\rangle_{\Delta E} \gg \langle\dot{n}_{\mathrm{c,s}}\rangle_{D} \Rightarrow \langle\dot{n}_{\mathrm{c,s}}\rangle = \langle\dot{n}_{\mathrm{c,s}}\rangle^{\mathrm{s}}_{D} \quad (18)$$

$$\langle\dot{n}_{\mathrm{c,s}}\rangle_{\Delta E} \ll \langle\dot{n}_{\mathrm{c,s}}\rangle_{D} \Rightarrow \langle\dot{n}_{\mathrm{c,s}}\rangle = \langle\dot{n}_{\mathrm{c,s}}\rangle^{\mathrm{s}}_{\Delta E}. \quad (19)$$

Based one the one-step global reaction of equation (1), the remaining surface reaction rates can be written as

$$\langle\dot{n}_{\mathrm{gp,gs}}\rangle = -\nu_{\mathrm{gp}}\langle\dot{n}_{\mathrm{o,gs}}\rangle, \quad \langle\dot{n}_{\mathrm{o,gs}}\rangle = \nu_{\mathrm{o}}\langle\dot{n}_{\mathrm{c,s}}\rangle, \quad (20)$$

where $\langle\dot{n}_{\mathrm{o,gs}}\rangle$ and $\langle\dot{n}_{\mathrm{gp,gs}}\rangle$ correspond to the rate of consumption of the oxygen and the production of the gaseous products in the gas phase (as a result of the heterogeneous reactions at the solid/gas interface).

For the volatile fuel component in the gas phase, the overall reaction rate $\langle\dot{n}_{\mathrm{v,g}}\rangle$ is written in terms of the production rate due to the pyrolysis and the consumption rate due to homogeneous reaction i.e.

$$\langle\dot{n}_{\mathrm{v,g}}\rangle = \langle\dot{n}_{\mathrm{v,g}}\rangle_{\mathrm{hom}}+\langle\dot{n}_{\mathrm{v,g}}\rangle_{\mathrm{pyr}}. \quad (21)$$

The first term in the above equation is written as

$$\langle\dot{n}_{\mathrm{v,g}}\rangle_{\mathrm{hom}} = \frac{M_i}{\nu_i'-\nu_i''}A_{\mathrm{g}}\langle\rho_{\mathrm{o,g}}\rangle\langle\rho_{\mathrm{v,g}}\rangle\exp\left(-\frac{\Delta E_{\mathrm{a,g}}}{R_{\mathrm{g}}\langle T\rangle^{\mathrm{g}}}\right), \quad (22)$$

where ν_v' and ν_v'' are the stoichiometric coefficients for the volatiles in the reaction model of equation (2) as a reactant ν_v' or product ν_v'' and M_v is the mean molecular weight of the volatiles. The rate of consumption of oxygen in the gas phase can then be determined from the stoichiometry of the gas-phase reaction as

† It has been suggested that wood pyrolysis should be represented as a process taking place at the surface which moves into the wood. However, X-ray and heat generation measurements in pyrolizing cellulosic cylinders indicate that reaction can take place throughout the volume at a rate dependent on the local temperature, so that the use of reaction kinetics cannot be discarded (Roberts [18]).

$$\langle \dot{n}_{o,g} \rangle = \left(\frac{M_o}{M_v}\right)\left(\frac{\nu'_v - \nu''_v}{\nu'_o - \nu''_o}\right)\langle \dot{n}_{v,g} \rangle_{hom}. \quad (23)$$

For the homogeneous reactions, $\Sigma_{i=1}^{n_g} \langle \dot{n}_{i,g} \rangle = 0$, i.e.

$$\langle \dot{n}_{o,g} \rangle + \langle \dot{n}_{v,g} \rangle + \langle \dot{n}_{gp,g} \rangle = 0. \quad (24)$$

In equation (21) $\langle \dot{n}_{v,g} \rangle_{pyr}$ represents the rate of volatile fuel release in the gas phase as a result of solid-phase pyrolysis $\langle \dot{n}_{v,s} \rangle$. Under the condition of a fast volatile diffusion/convection through the particles and a negligible mass transfer resistance at the surface of the particles, we have

$$\langle \dot{n}_{v,g} \rangle_{pyr} = -\langle \dot{n}_{v,s} \rangle.$$

This scheme also requires the condition of a rapid mixing of the gas in the pores. This assumption is appropriate because of the small pore sizes, high gas velocity (at the pore level) and boundary-layer break up for the gas flow through a random arrangement of small particles. However, if this condition cannot be met, the rate at which volatiles are released in the gas phase can be adjusted by setting the exponent n in equation (14) to a value larger than one. The higher the values of n, the slower the rate of the mass transfer of the volatiles to the gas phase.

2.3. *Effective transport properties*

The specific interfacial gas/solid surface area for a packed bed of spherical particles is $A_{sg}/V = 6(1-\varepsilon)/d_p$. The interstitial Nusselt number ($Nu_d = hd_p/\langle k \rangle^g$, based on the particle diameter and the gas productivity) is (Wakao and Kaguei [19])

$$\langle Nu_d \rangle_{A_{gs}} = 2 + 1.1 Re_d^{0.6} Pr^{0.33}. \quad (25)$$

The Reynolds and Prandtl numbers are defined as $Re_d = \varepsilon \langle u \rangle^g d_p/\nu_g$ and $Pr = \nu_g/\alpha_g$, respectively, and α_g is the thermal diffusivity of the gas phase. The axial thermal dispersion coefficient D^d_{xx}, which is a function of the thermal Peclet number Pe_t based on the particle diameter, is given by Kaviany [17]

$$D^d_{xx} = \alpha_g \left[\frac{3}{4} Pe_t + \frac{1}{6}\pi^2 (1-\varepsilon) Pe_t \ln Pe_t\right], \quad (26)$$

where $Pe_t = \varepsilon \langle u \rangle^g d_p/2\alpha_g$.

The radiative heat transfer is assumed to occur among the opaque surface of the particles and the gas is treated as nonparticipating, i.e. the radiative energy is emitted, absorbed, and scattered by the particles. By treating the packed bed as a continuum in the optically-thick limit the radiative heat conductivity is (Kaviany [17])

$$\langle k_r \rangle^s = 4 F d_p \sigma \langle T \rangle^{s^3}. \quad (27)$$

For opaque spherical particles, the radiant exchange factor F depends on $\langle k \rangle^s$, ε, surface radiation properties (i.e. emissivity ε_r) and to a lesser degree the extent of specular reflection. The radiation exchange factor has been correlated (Singh and Kaviany [20]) as

$$F = k_r^* = \frac{k_r}{4 d_p \sigma \langle T \rangle^{s^3}} = a_{F1} \varepsilon_r \tan^{-1}\left(a_{F2} \frac{k_s^{* a_{F3}}}{\varepsilon_r}\right) + a_{F4},$$

$$k_s^* = \frac{k_s}{4 d_p \sigma \langle T \rangle^{s^3}}. \quad (28)$$

For a diffuse surface, the values for a_i are 0.5756, 1.535, 0.8011 and 0.1843.

In the gas-phase, the total mass diffusivity is written as the sum of molecular diffusivity D and the axial mass dispersion coefficient defined similar to the thermal dispersion coefficient as

$$D^d_{m_{xx}} = D\left[\frac{3}{4} Pe_m + \frac{1}{6}\tau^2 (1-\varepsilon) Pe_m \ln Pe_m\right], \quad (29)$$

where $Pe_m = \varepsilon \langle u \rangle^g d_p/2D$.

The interstitial mass transfer Sherwood number is of the form (Wakao and Kaguei [19])

$$\langle Sh_d \rangle_{A_{gs}} = 2 + 1.1 Re_d^{0.6} Sc^{0.33}. \quad (30)$$

The Schmidt number Sc, is defined as $Pr = \nu_g/D$.

2.4. *Solution method*

The governing equations for the conservation of energy and species are discretized in the finite-volume form [21]. A nonuniform mesh distribution with a higher concentration of the nodal points near the combustion front is used. Constant properties are assumed, except for the temperature dependence of the radiative conductivity, the gas density and binary mass diffusion. The power-law scheme describes the fluxes of species and heat at the finite control-volume faces. The species and temperature distributions, as well as the propagation velocity of the reaction front, are solved iteratively, prescribing an inlet gas flow and a front speed which depend on the final equilibrium temperature through the integrated energy and mass equations. The reaction rates are linearized to achieve stability during the iterations.

Since the propagation speed is not known *a priori*, the location of the front is fixed by specifying the temperature (in the solid-phase) at a point in the computational domain. This scheme avoids the cold boundary difficulty. The location at which the solid temperature is fixed is chosen in such a way to ensure that species and temperatures gradients nearly vanish at the cold boundary; otherwise heat loss will occur through this boundary. Species distribution are initially computed using an assumed linear temperature distribution as the initial solution profile. When a converged solution is obtained for the gaseous and solid species distribution, the energy equation for the solid and gas are included in the iteration. The energy equations are solved using the latest species distributions. The convergence criterion, adopted for both the species and temperature distribution, is less than 10^{-7}.

The thermophysical properties and the kinetic rate

Table 1. Thermochemicophysical properties used in the computations

		Gas	Other	Solid
c_p	kJ kg K^{-1}	1.05	—	2.81
k	Wm K^{-1}	26.3×10^{-3}	—	0.15
ρ	kg m^{-3}	1.16	—	663
D	m^2 s^{-1}	2.1×10^{-5}	—	—
Δi	MJ kg^{-1} Fuel	4.6	14	9.4
v_o	kg O_2 kg^{-1} Fuel	—	1.25	—
F	—	—	0.68	—
d_p	m	—	6.4×10^{-3}	—
ΔE_p	kJ mol^{-1}		—	75.3
A_p	s^{-1}		—	2.5×10^4
ΔE_c	kJ mol^{-1}		—	163
A_c	s^{-1}		—	5.67×10^9
ΔE_g	kJ mol^{-1}	143.5	—	—
A_g	s^{-1}	10^9	—	—

constants used in the computations are given in Table 1. The amount of oxygen required for the stoichiometric burning of wood, v_o, is 1.25 kg O_2/kg fuel (Tillman *et al.* [22]). The heat of combustion for wood measured in a bomb calorimeter (Fatehi and Kaviany [11]) is 14 MJ kg^{-1} fuel. Note that in the bomb calorimeter the entire combustible matter is consumed. Assuming that the initial volatile content of the wood particle is 45% (yielding 55% char), the heat of combustion for the volatiles, $\Delta i_{v,g}$ and for the char, $\Delta i_{c,s}$, is taken to be 10.24 MJ kg^{-1} volatile and 17.1 MJ kg^{-1} char, respectively. Shafizadeh [15] reports that for various types of wood, the ratio of the heat of combustion of the volatile products to that of the char is typically 50–60%, whereas the ratio of the volatiles yield to the char yield in the pyrolysis products varies from 41 to 85%. The heat of pyrolysis, $\Delta i_{v,s}$, is taken to be 0.7 MJ kg^{-1} fuel (Kansa *et al.* [23]). The kinetic rate constants for the char oxidation are given by Kashiwagi and Nambu [14]. Kansa *et al.* [23] provide the pre-exponential frequency factor and the activation energy for the pyrolytic reactions in wood. For the gas-phase oxidation, the kinetic rate constants are taken to be 10^9 s^{-1} for the pre-exponential factor, and 143 kJ mol^{-1} for the activation energy.

3. RESULTS AND DISCUSSION

The pyrolytic reaction is initiated ahead of the char oxidation region, generating the volatile fuel to burn in the gas phase further downstream. In contrast to the char and gas-phase oxidations which are oxygen limited, the volumetric pyrolysis is assumed to occur in the presence of nitrogen, provided the temperature is high enough. As such, pyrolysis region may extend over the char oxidation region. This indicates that while the char oxidation is taking place at the surface of the particle, the pyrolysis may still continue in the interior of the particle. The spatial density variations

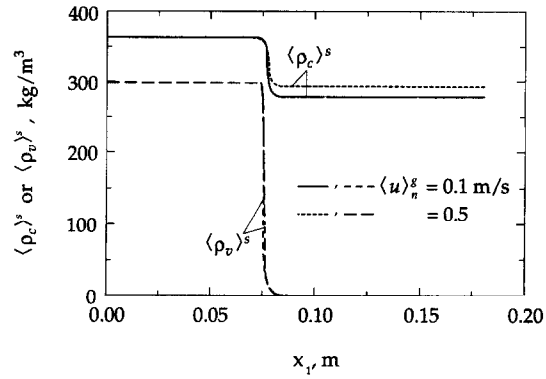

Fig. 3. Spatial distribution of the volatiles and the char densities in the solid phase for two air pore velocities, $\langle u\rangle_n^g = 0.1$ and 0.5 m s^{-1}.

of the char and the volatiles in the condensed phase, are shown in Fig. 3.

It is evident that the gasification takes place at a much faster rate than the char oxidation. In fact, pyrolysis of the volatile species on the particle is nearly complete at the start of the char oxidation. The density variations are computed for the incoming gas pore velocities of $\langle u\rangle_n^g = 0.1$ and 0.5 m s^{-1}. The flow rate of the incoming air has negligible effect on the thickness of the pyrolysis region. In contrast to the char oxidation, the pyrolysis is independent of the oxygen concentration in the gas and its availability. The only dependency that the volumetric pyrolysis exhibits is on the local solid temperature in the presence of nitrogen. Figure 4 presents the temperature and the volatile density variations in the solid phase along the fuel bed for $\langle u\rangle_n^g = 0.1$ m s^{-1}. For wood particles, pyrolysis temperature is typically 625–635 K. As is evident from Fig. 4, most of the solid gasification takes place within this range of temperatures in the packed bed. It is interesting to note that since the temperature gradient within the pyrolysis region does not change significantly with variations in the incoming gas flow rate, the concentration of the volatiles in the con-

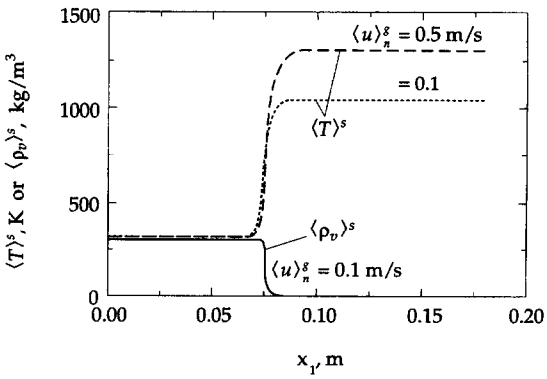

Fig. 4. The predicted variation of the temperature and volatiles density in the solid phase, showing the domains of the pyrolysis and the preheating regions for $\langle u\rangle_n^g = 0.1$ and 0.5 m s^{-1}.

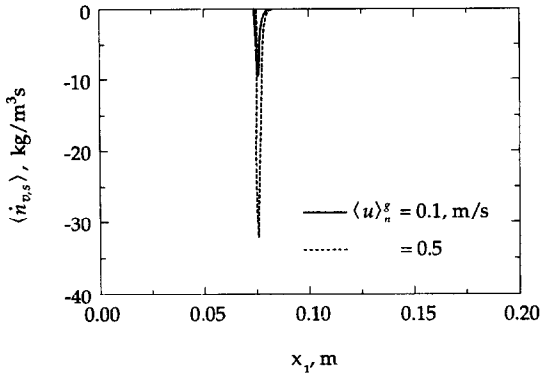

Fig. 5. The predicted effect of the air pore velocity on the pyrolysis rate for $\langle u \rangle_n^g = 0.1$ and 0.5 m s^{-1}.

densed phase also remains unaffected by the gas pore velocity (Fig. 3).

The solid volatization rates $\langle \dot{n}_{v,s} \rangle$ for the gas velocities of 0.1 and 0.5 m s^{-1} are plotted in Fig. 5. The thickness of the pyrolysis region remains nearly the same for the two velocities even though the maximum pyrolysis rate for the higher velocity is substantially larger than that for the lower velocity. This implies that most of the volatiles are released from the solid into the gas prior to the char oxidation, leaving behind only trace amounts of the volatiles in the solid. Even for the remaining low concentration of the volatiles, higher solid temperatures in the oxidation region at the higher gas velocities, leads to higher peak gasification rates and extends the pyrolysis region into the char oxidation region.

Figure 6 shows the spatial distribution of the mass fraction of the oxygen and the volatile fuel in the gas phase, as well as the variation of the condensed phase density ($\langle \rho \rangle^s = \langle \rho_c \rangle^s + \langle \rho_v \rangle^s$) normalized with respect to the nonreacted solid density $\langle \rho \rangle_n^s$. The reduction in the solid density is a result of the heterogeneous reactions with the attack of the oxygen in the surface of the solid fuel. Oxygen consumption is a result of the two competing heterogeneous and homogeneous reactions in the basis of their relative kinetics and the reaction rates. The volatile fuel concentration in the gas phase initially increases ahead of the char oxidation front due to the pyrolysis, and then diminishes as a result of its reaction with the oxygen in the gas phase. Unburnt volatile fuel remains in the post gas-phase oxidation region, where the reaction is chemically frozen due to the absence of oxygen. Similarly, the solid density remains unchanged in the post-heterogeneous oxidation region.

The concentration of the unburnt volatile fuel in the flue gas leaving the system is reduced when the air flow rate increases. Thus, the total consumption of the unburnt volatiles in the gaseous products can be reached when the air supply is increased to the limit of the stoichiometry of the gas-phase reaction $\langle u \rangle_{n,st}^g$. For air velocities higher than $\langle u \rangle_{n,st}^g$, the excess oxygen can then participate in the heterogeneous reactions to consume more solid. For air velocities lower than $\langle u \rangle_{n,st}^g$, solid consumption decreases as the air velocity increases. This implies that the oxygen is preferentially consumed in the gas phase because the kinetic rates of the homogeneous reactions are considerably higher than the rate of the oxygen mass diffusion to the solid surface. Reaction kinetics solely dictate the distribution of the oxygen between the two reaction pathways.

The intensity, thickness, and position of each of the reactions within the combustion wave structure are illustrated in Fig. 7. The order of the appearance and the extent of each reaction correspond to the Arrhenius kinetics that it follows. It is interesting to note that for $\langle u \rangle_n^g = 0.1$ m s^{-1}, the gas/solid reaction appears to be on the same order of magnitude as the gas-phase reaction. For the higher velocity of $\langle u \rangle_n^g = 0.5$ m s^{-1}, the gas-phase reaction is more dominant over the heterogeneous reaction. This is in accord with the general observation of the transition from smoldering to flaming in the reverse combustion, when air supply increases.

Figure 8 shows the temperature distribution along the fuel bed in the gas and solid phases for the gas pore velocities of $\langle u \rangle_n^g = 0.1$ and 0.5 m s^{-1}. The con-

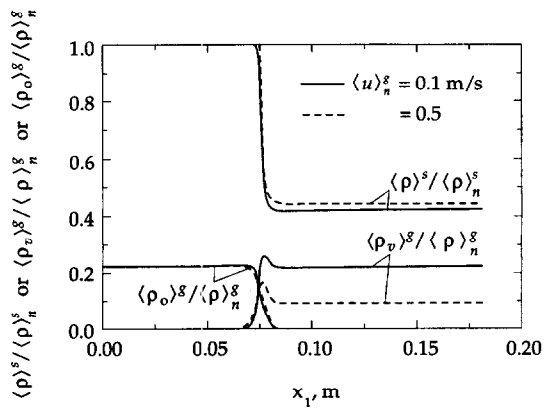

Fig. 6. The predicted effect of the air pore velocity on the species distribution in the gas and solid phases for $\langle u \rangle_n^g = 0.1$ and 0.5 m s^{-1}.

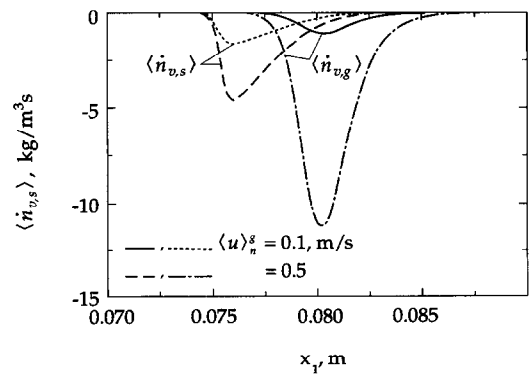

Fig. 7. Magnified view of the predicted reaction rates for the char and gas-phase oxidation regions for the air pore velocities of $\langle u \rangle_n^g = 0.1$ and 0.5 m s^{-1}.

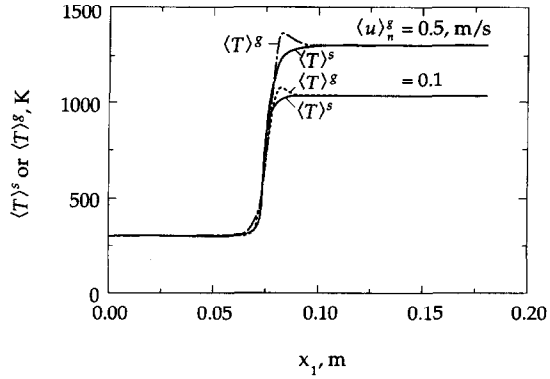

Fig. 8. The predicted spatial variation of the gas and solid phase temperatures for the air pore velocities of $\langle u\rangle_n^g = 0.1$ and 0.5 m s^{-1}.

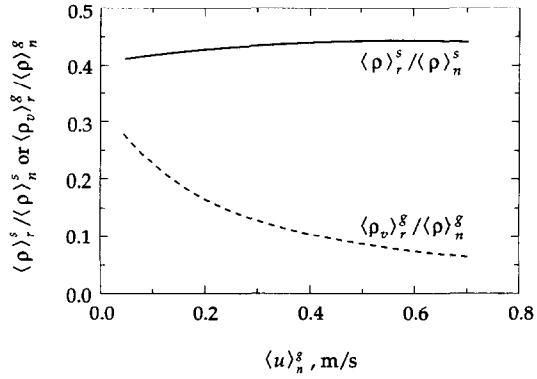

Fig. 10. The predicted effect of the air pore velocity on the final normalized char and volatiles densities in the chemically frozen region.

dition of local thermal equilibrium between the gas and solid phases breaks down in the reaction region. In this region, due to the lack of thermal equilibrium, heat is exchanged between the effective gas and solid media. The transfer of some of the heat through the solid to the reactants in the gas phase causes a temperature increase in the flame (and in turn, heat transfer to the solid). The gas-phase thus exhibits a local temperature in the reaction region higher than the final equilibrium temperature for the chemically frozen limit. This excess temperature is determined solely by the proportion of heat recirculated through the effective solid medium, the excess temperature (or enthalpy) in the gas phase becomes more significant as the incoming air flow rate increases. In the post-reaction regime, the gaseous products and the remaining solid must reach the normal final temperature (determined by the amount of consumed solid and volatile fuel) because the system is considered to be adiabatic. As is evident from Fig. 8, the gas- and solid-phase temperatures throughout the combustion wave structure increase as air velocity increases.

The effect of the air pore velocity on the density of the remaining char in the condensed phase in the post-char oxidation region, $\langle\rho_{c,s}\rangle_r$, is shown in Fig. 9. The higher air flow rates result in a lower consumption of the solid phase. With the increased temperature in the gas phase at higher air flow rates and the increased intensity of the gas-phase reactions, the oxygen availability for the surface reactions diminishes. This in turn results in a lower consumption of the char in the condensed phase. From Fig. 9, it is apparent that the char density approaches an asymptote for the air pore velocities greater than 0.7 m s^{-1}.

Figure 10 illustrates the effect of the air pore velocity on the density of the condensed phase (normalized with respect to the nonreacted solid density) and the mass fraction of the volatile fuel in the gas-phase in the post-oxidation (gas and solid) region. While the solid density reaches a constants value, signifying no char consumption, the concentration of the unburnt volatile fuel in the gaseous products reduces as the air supply increases.

The reduction in the volatile content of the flue gas is expected to continue until $\langle u\rangle_n^g$ reaches $\langle u\rangle_{n,st}^g$. The generated heat from the homogeneous reaction increases the final equilibrium temperature $\langle T\rangle_r^s = \langle T\rangle_r^g$, up to the point of gas-phase stoichiometry where $\langle\rho_v\rangle_r^g = \langle\rho_o\rangle_r^g = 0$. For $\langle u\rangle_n^g > \langle u\rangle_{n,st}^g$, the reaction of the condensed phase

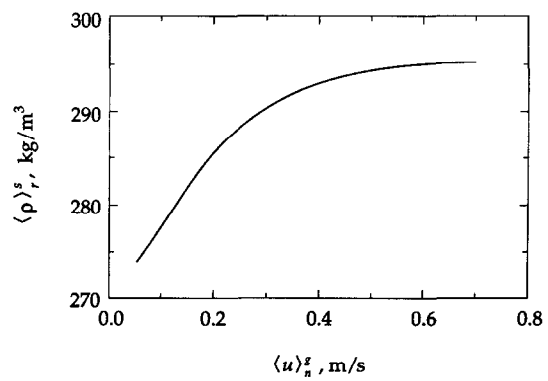

Fig. 9. The predicted effect of the air pore velocity on the density of the remaining solid in the post-oxidation region for $\langle u\rangle_n^g = 0.1$ and 0.5 m s^{-1}.

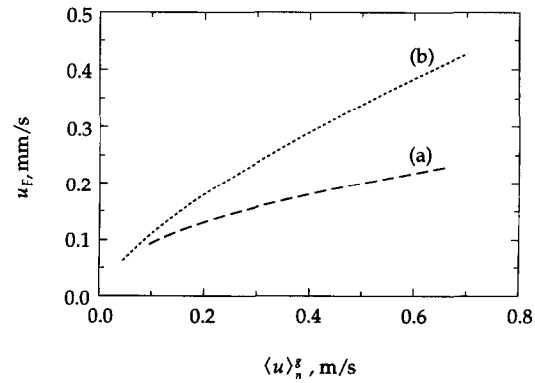

Fig. 11. The predicted variation of the front speed with respect to the air pore velocity for: (a) $\Delta i_{v,g}/\Delta i_{c,s} = 0.25$, $\langle\rho_v\rangle_n^s/\langle\rho\rangle_n^s = 0.15$, $\Delta E_{a,g} = 163$ kJ mol^{-1}, $A_g = 10^9$ s^{-1}; and (b) $\Delta i_{v,g}/\Delta i_{c,s} = 0.6$, $\langle\rho_v\rangle_n^s/\langle\rho\rangle_n^s = 0.45$, $\Delta E_{a,g} = 143$ kJ mol^{-1}, $A_g = 10^9$ s^{-1}.

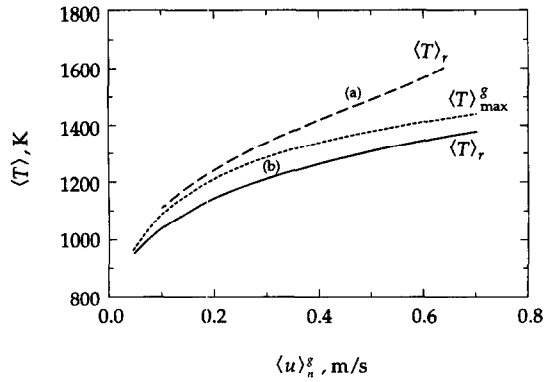

Fig. 12. The predicted variation of the adiabatic final temperature $\langle T\rangle_r$ and the maximum gas temperature $\langle T\rangle^g_{max}$, as a function of the air pore velocity for: (a) $\Delta i_{v,g}/\Delta i_{c,s} = 0.25$, $\langle \rho_v\rangle^s_n/\langle\rho\rangle^s_v = 0.15$, $\Delta E_{a,g} = 163$ kJ mol^{-1}, $A_g = 10^9$ s^{-1}; and (b) $\Delta i_{v,g}/\Delta i_{c,s} = 0.6$, $\langle \rho_v\rangle^s_n/\langle\rho\rangle^s_n = 0.45$, $\Delta E_{a,g} = 143$ kJ mol^{-1}, $A_g = 10^9$ s^{-1}.

with the excess oxygen generates the additional heat too continue the rise in the temperature of the gas and solid phases. The air flow rates required for the gas-phase and solid-phase stoichiometry (i.e. $\langle\rho_{c,s}\rangle = \langle\rho_{v,s}\rangle = \langle\rho_v\rangle^g = 0$) to be reached, may be beyond the limit of reaction front extinction (due to the convective cooling) or fluidization of the packed bed. This needs to be investigated in future studies for air flow rates higher than the limits considered in the present analysis.

Due to the uncertainty in the initial volatile content of the wood particles and the distribution of the heat of combustion of the pyrolysis products (as char and combustible volatiles), as well as the kinetic rate constants for the gas phase oxidation, two sets of parameters are included in the study of the effect of the air pore velocity on the propagation speed and the final equilibrium temperature, namely, (a) $\Delta i_{v,g}/\Delta i_{c,s} = 0.25$, $\langle \rho_v\rangle_{sn}/\langle\rho\rangle^s_n = 0.15$, $\Delta E_{a,g} = 163$ kJ mol^{-1}, $A_g = 10^9$ s^{-1} and (b) $\Delta i_{v,g}/\Delta i_{c,s} = 0.6$, $\langle \rho_v\rangle_{sn}/\langle\rho\rangle^s_n = 0.45$, $\Delta E_{a,g} = 143$ kJ mol^{-1}, $A_g = 10^9$ s^{-1}. The variation of the propagation speed with respect to the incoming air pore velocity is shown in Fig. 11 for the two parameter sets. The rate of propagation is set by the balance between the rate of the generated heat (the heat produced in the exothermic char and gas oxidations minus the endothermic heat of pyrolysis) and the rate of heat transfer to the nonreacted fuel element. The rate of heat generation is proportional to the rate of oxygen supply.

Figure 12 presents the variation of the final equilibrium temperature $\langle T\rangle_r = \langle T\rangle^s_r = \langle T\rangle^g_r$ and the maximum attainable temperature in the gas phase $\langle T\rangle^g_{max}$, with respect to the incoming air pore velocity. For the low velocity of $\langle u\rangle^g_n = 0.05$ m s^{-1} the temperature difference between the gas medium and the solid phase is negligible. With increasing the air flow rate, the difference between $\langle T\rangle^g_{max}$ and $\langle T\rangle_r$ increases up to the approximate velocity of $\langle u\rangle^g_n = 0.4$ m s^{-1}, beyond which it remains roughly constant. Figure 12 also indicates that the rate of temperature rise in the gas and solid phases decays as the air supply increases,

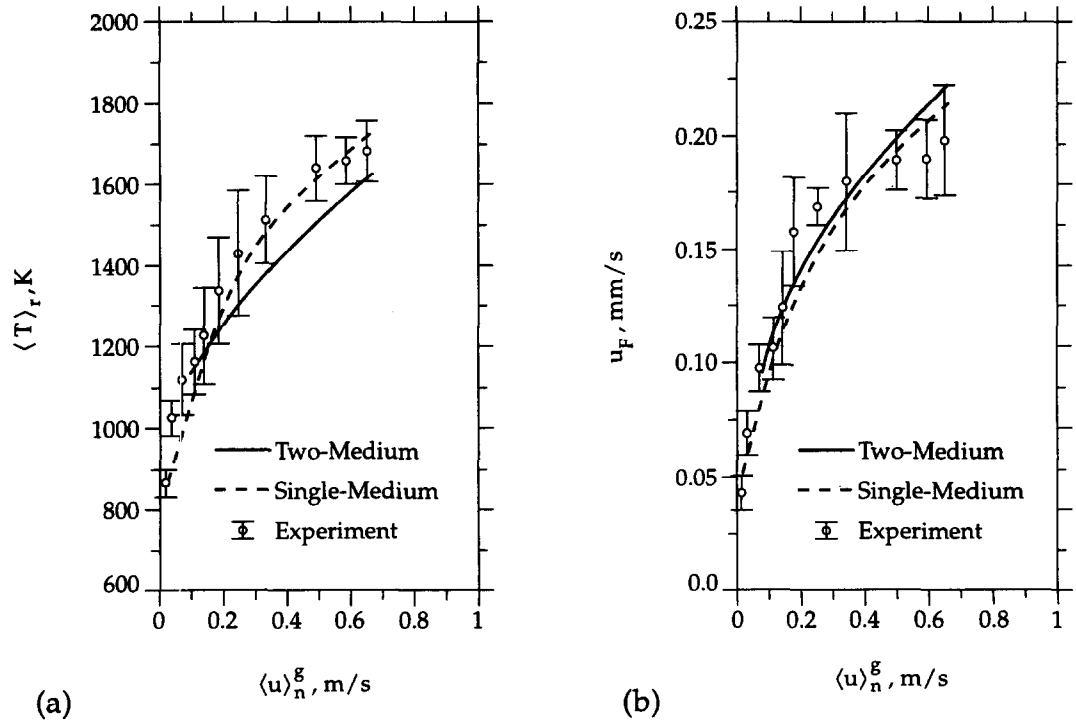

Fig. 13. Variation of: (a) the adiabatic final temperature; and (b) the front speed, with the air pore velocity for the oxygen-limited regime. The experimental results are shown along with the predicted results of the single-medium and two-medium models.

in a manner similar to the decay of the char consumption, but at higher air velocities.

Figure 13 presents the results obtained previously (Fatehi and Kaviany [11]) for the single-medium treatment of reverse combustion (assuming thermal equilibrium between the phases) in a packed bed of wood particles, as well as the experimental results, in comparison to the present computational values for the propagation speed and the final equilibrium temperature. An agreement between the experimental observations and the results of this study can be achieved when the properties corresponding to the parameter set (a) are used in the two-medium treatment of reverse combustion.

4. CONCLUSIONS

In order to estimate the effect of the gas-phase reaction and the extent of the local thermal nonequilibrium between the gas and the solid phases, the two-medium treatment of the reverse combustion for the system of air flowing through a packed bed of wood particles is made. The role of gas-phase oxidation co-existing with the gas–solid surface reaction is examined parametrically while keeping the total specific released energy constant. The results indicate that thermal nonequilibrium is most significant in the reaction region. It is also found that the inclusion of the gas-phase oxidation in the reverse smoldering models substantially influences the propagation speed and solid conversion. For the low air flow rates, the mass-diffusion controlled heterogeneous reaction is dominant over the gas-phase oxidation. As the air flow rate increases, both the front speed and the temperature increase. At high temperatures, the gas-phase oxidation becomes significant and transition to flaming occurs. Preferential consumption of the oxygen in the gas phase reduces the consumption rate of the solid. It is predicted that the oxygen is completely consumed within the reaction region leaving unburnt volatiles and char in the post-oxidation region.

REFERENCES

1. Palmer, K. M., Smouldering combustion in dusts and fibrous materials. *Combustion and Flame*, 1957, **1**, 129.
2. Ohlemiller, T. J., Modelling of smoldering combustion propagation. *Progress in Energy Combustion Science*, 1985, **11**, 277.
3. Ohlemiller, T. J., Forced smolder propagation and the transition to flaming in cellulosic insulation. *Combustion and Flame*, 1990, **81**, 354.
4. Rogers, F. E. and Ohlemiller, T. J., Smolder characteristics of flexible polyurethane foams. *Journal of Fire and Flammability*, 1980, **11**, 32.
5. Moussa, N. A., Toong, T. Y. and Garris, C. A., Mechanism of smoldering of cellulosic materials. *Proceedings of the 16th Symposium (International) on Combustion*, The Combustion Institute, 1976.
6. Dosanjh, S. S., Pagni, P. J. and Fernandez-Pello, A. C., Forced concurrent smoldering combustion. *Combustion and Flame*, 1987, **68**, 131.
7. Schult, D. A., Matkowsky, B. J., Volpert, V. A. and Fernandez-Pello, A. C., Propagation and extinction of forced opposed flow smolder waves. *Combustion and Flame*, 1995, **101**, 471.
8. Robinovich, O. S. and Gurevich, F. G., Low-temperature technological combustion of porous systems with forced filtration of a gas reagent. *International Journal of Heat and Mass Transfer*, 1986, **29**, 241.
9. Britten, J. A. and Krantz, W. B., Linear stability of planar reverse combustion in porous media. *Combustion and Flame*, 1985, **60**, 125.
10. Britten, J. A. and Krantz, W. B., Asymptotic structure of planar nonadiabatic reverse combustion fronts in porous media. *Combustion and Flame*, 1986, **65**, 51.
11. Fatehi, M. and Kaviany, M., Adiabatic reverse combustion in a packed bed. *Combustion and Flame*, 1994, **99**, 1.
12. Lozinski, D. and Buckmaster, J., Quenching of reverse smolder. *Combustion and Flame*, 1995, **102**, 87.
13. Ohlemiller, T. J., Smoldering combustion propagation through a permeable horizontal fuel layer. *Combustion and Flame*, 1990, **81**, 341.
14. Kashiwagi, T. and Nambu, H., Global kinetic constants for thermal oxidative degradation of a cellulosic paper. *Combustion and Flame*, 1992, **88**, 345.
15. Shafizadeh, F., The chemistry of pyrolysis and combustion. In *The Chemistry of Solid Wood*, ed. R. Rowell. ACS, Washington D.C. 1984, p. 489.
16. Kosdon, F. J., Williams, F. A. and Buman, C., Combustion of vertical cellulosic cylinders in air. *Proceedings of the 12th Symposium (International) on Combustion*, 1968, p. 253.
17. Kaviany, M., *Principles of Heat Transfer in Porous Media*, 2nd edn. Springer, New York, 1995.
18. Roberts, F. E., A review of kinetics data for the pyrolysis of wood and related substances. *Combustion and Flame*, 1970, **14**, 261.
19. Wakao, N. and Kaguei, S., *Heat and Mass Transfer in Packed Beds*. Gordon and Breach, New York, 1982.
20. Singh, B. and Kaviany, M., Effect of solid conductivity on radiative heat transfer in packed beds. *International Journal of Heat and Mass Transfer*, 1994, **37**, 2579.
21. Patankar, S. V., *Numerical Heat Transfer and Fluid Flow*. Hemisphere, Washington, D.C., 1980.
22. Tillman, D. A., Rossi, A. J. and Kitto, W. D., *Wood Combustion: Principles, Processes and Economics*. Academic, New York, 1981.
23. Kansa, E. J., Perlee, H. E. and Chaiken, R. F., Mathematical model of wood pyrolysis including internal forced convection. *Combustion and Flame*, 1977, **29**, 311.